Temperature effects in topological insulators of transition metal dichalcogenide monolayers

Siyu Chen [1,*] Isaac J. Parker [2] and Bartomeu Monserrat [1,3,†]

[1]*TCM Group, Cavendish Laboratory, University of Cambridge, J. J. Thomson Avenue, Cambridge CB3 0HE, United Kingdom*
[2]*Gonville and Caius College, University of Cambridge, Trinity Street, Cambridge CB2 1TA, United Kingdom*
[3]*Department of Materials Science and Metallurgy,
University of Cambridge, 27 Charles Babbage Road, Cambridge CB3 0FS, United Kingdom*

We investigate the role of temperature on the topological insulating state of metal dichalcogenide monolayers, 1T′-MX_2 (M = W, Mo and X = S, Se). Using first principles calculations based on density functional theory, we consider three temperature-related contributions to the topological band gap: electrons coupling with short-wavelength phonons, with long-wavelength phonons *via* Fröhlich coupling, and thermal expansion. We find that electron-phonon coupling promotes the topology of the electronic structures of all 1T′-MX_2 monolayers, while thermal expansion acts as a counteracting effect. Additionally, we derive the band renormalization from Fröhlich coupling in the two-dimensional context and observe its relatively modest contribution to 1T′-MX_2 monolayers. Finally, we present a simplified physical picture to understand the "inverse Varshni" effect driven by band inversion in topological insulators. Our work reveals that, among the four 1T′-MX_2 studied monolayers, $MoSe_2$ is a promising candidate for room-temperature applications because its band gap displays remarkable resilience against thermal expansion, while the topological order of WS_2 can be tuned under the combined influence of strain and temperature. Both materials represent novel examples of temperature-promoted topological insulators.

I. INTRODUCTION

In condensed-matter physics, the unique electronic properties of topological insulators have sparked immense interest, captivating the scientific community with their potential to redefine the landscape of electronic and quantum computing technologies. Over the past two decades, significant advancements have been made in unravelling the fundamental features of topological insulators and in the manipulation of their distinctive properties [1–8].

The manipulation of topologically nontrivial band gaps has emerged as a highly active research direction. These manipulations have been achieved through various means, including alterations in chemical composition [9,10], the application of external pressure [11,12], the imposition of mechanical strain [13–15], and the influence of electromagnetic fields [16–18]. Recent attention within the scientific community has shifted towards exploring the intriguing possibility of controlling the topological characteristics of these materials through temperature, both in theory [19–28] and experiments [29–37].

Despite this burgeoning interest, a comprehensive examination of the interplay between temperature and the unique electronic states of topological insulators remains a relatively under-explored frontier. So far, most works indicate that increasing temperature suppresses the topological phase, in the sense that the topological band gap decreases with increasing temperature [21,23,25,26,28,36,37]. In particular, thermal expansion is often responsible for the ultimate suppression of topological order because it drives the system towards the atomic limit. This suggests that a generic topological phase diagram as a function of temperature is one with a low-temperature topological phase and a high-temperature normal phase. Indeed, several reports describe the reduction of the topological band gap with increasing temperature culminating in a transition from a topological (crystalline) insulator into a normal insulator [21,25,26,30] or from a strong topological insulator into a weak topological insulator [23,36,37]. It has been argued that electron-phonon interactions can promote a topological insulating phase with increasing temperature in BiTlS [22] and bismuthene [27], but these works neglect thermal expansion so the overall temperature dependence in these materials remains an open question. As far as we are aware, the only compound in which temperature has been shown to promote topological order, specifically a topological semimetallic phase, is PbO_2 [24], and there are no examples in which increasing temperature promotes a topological insulating phase.

Motivated by the paucity of reports on materials where temperature promotes topological insulating states, in this work we systematically study the interplay between temperature and topology in four transition-metal dichalcogenide (TMD) monolayers 1T′-MX_2 (where M = W, Mo and X = Se and S). The motivation behind the choice of monolayer

*sc2090@cam.ac.uk
†bm418@cam.ac.uk

TMDs for our study is twofold. First, monolayer materials often exhibit unconventional thermal effects, including weak or negative thermal expansion, which may minimize the detrimental effects of thermal expansion on topological order observed in most compounds. Second, these specific TMD monolayers have been shown to be a realization of topological insulators at 0 K [38,39] with a strong band inversion feature, but their behavior at finite temperature is still an open question.

Our investigation illustrates the pivotal role played by electron-phonon coupling and thermal expansion in influencing the topology of the electronic structures of $1\text{T}'$-MX_2 monolayers. Particularly noteworthy are $MoSe_2$ and WS_2, which stand out as the first examples of temperature-promoted topological insulators. The former emerges as a promising candidate for room-temperature applications owing to its remarkable resistance to thermal expansion, while the latter exhibits a tunable topological behavior when subjected to the combined influence of strain and temperature. Overall, our findings enrich the family of materials where temperature can promote topology.

The paper is organized as follows: In Sec. II, we present the theory of finite-temperature band structures and its first principles implementation in the context of the finite-difference method. In Sec. III, we apply the method to investigate $1\text{T}'$-MX_2, showcasing the competition between electron-phonon coupling and thermal expansion. In Sec. IV, we propose a simple model that aids in understanding the circumstances under which electron-phonon coupling can promote the topological phase in the presence of significant band inversion. In Sec. V, we show that the topological order of WS_2 can be manipulated through a combination of strain and temperature, illustrating a transition from a low-temperature normal to a high-temperature topological phase. Finally, we summarize the contributions and findings of our research in Sec. VI.

II. TEMPERATURE-DEPENDENT TOPOLOGICAL BAND GAP

A topological phase transition induced by temperature from a topological insulator to a trivial insulator (or the other way around) requires the bulk band gap to re-order. In the case of centrosymmetric materials, the band re-ordering is mediated by a gapless Dirac semimetal phase [40], where the Dirac cone is located at one of the time-reversal-invariant momentum points. Therefore, the key to exploring the role of temperature in topological insulators is to consider the temperature dependence of certain energy eigenvalues.

The temperature-dependent eigenenergy $E_{nk}(T)$ of a single electron with band index n and wave vector $\mathbf{k}$ can be approximated by the sum of two independent contributions: the renormalization of the eigenenergy by electron-phonon interactions, $\Delta E_{nk}^{\text{EP}}(T)$; and by thermal expansion, $\Delta E_{nk}^{\text{TE}}(T)$. For practical calculation reasons, the former needs to be further decomposed into the short- and long-wavelength phonon contributions, $\Delta E_{nk}^{\text{S}}(T)$, and $\Delta E_{nk}^{\text{L}}(T)$, each treated separately. Overall, the total shift of the electron eigenenergy at

temperature T reads

$$\Delta E_{nk}(T) = \Delta E_{nk}^{\text{S}}(T) + \Delta E_{nk}^{\text{L}}(T) + \Delta E_{nk}^{\text{TE}}(T). \quad (1)$$

In the following sections, we discuss each contribution in turn. We use atomic units, $\hbar = e = m_{\text{el}} = 4\pi\epsilon_0 = 1$, unless otherwise stated.

A. Band gap renormalized by short-wavelength phonons

The investigation of band renormalization through coupling electrons to short-wavelength phonons has a long history, culminating in the well-established Allen-Heine-Cardona (AHC) theory [41–43]. The AHC theory can be reformulated in a manner that can readily lend itself to implementation within the first-principles finite-difference method:

$$\Delta E_{nk}^{\text{S}}(T) = \frac{1}{2} \sum_{\nu\mathbf{q}} \frac{1}{2\omega_{\nu\mathbf{q}}} \frac{\partial^2 E_{nk}}{\partial \mu_{\nu\mathbf{q}}^2} [1 + 2n_{\text{B}}(\omega_{\nu\mathbf{q}}, T)], \quad (2)$$

where $\omega_{\nu\mathbf{q}}$ is the frequency of a phonon with the branch number ν and wave vector $\mathbf{q}$, $\mu_{\nu\mathbf{q}}$ is the real-valued phonon displacement [see the detailed definition in Eqs. (A1) and (A4)], and $n_{\text{B}}(\omega_{\nu\mathbf{q}}, T) = [\exp(\frac{\omega_{\nu\mathbf{q}}}{k_{\text{B}}T}) - 1]^{-1}$ is the Bose-Einstein factor. It is worth noting that there is a nonzero correction to the energy band even at zero temperature with the vanishing Bose-Einstein factor, arising from the zero-point motion of the ions as a purely quantum effect. We refer readers who are interested in the rigorous mathematical derivations of the theory to Refs. [41–46], where the same results have been obtained through alternative approaches. We show the equivalence between our formulation and others in Appendix A.

B. Band gap renormalized by long-wavelength phonons

In principle, Eq. (2) captures the coupling between electrons and *all*-wavelength phonons. However, in practice, explicitly accessing the $\mathbf{q}$ points close to the center of the Brillouin zone (BZ) can become computationally prohibitive due to the inherent incompatibility of the long-wavelength limit with the Born-von Kármán periodic boundary condition. As a result, accounting for the band-gap renormalization contributed by long-wavelength phonons requires a separate treatment.

Specifically, in the long-wavelength limit, the significance of atomic-scale interactions diminishes, and electrons can be regarded as becoming coupled with the macroscopic electric field induced by longitudinal optical phonons. This mechanism is known as the Fröhlich interaction [47,48]. It is especially crucial in the case of ionic crystals, where the interaction has been shown to be strong enough to significantly influence physical phenomena such as electron lifetimes and carrier mobilities [49].

Nery and Allen derived an analytical expression to address the missing portion of the contribution associated with the long-wavelength optical phonon modes for three-dimensional (3D) materials [50]. Following a similar methodology, combined with the latest results on polarons in two-dimensional (2D) systems [51,52], we have derived the corresponding

band-gap renormalization for a 2D material:

$$\Delta E_{n\mathbf{k}}^{\mathrm{L}}(T) = \int_0^\infty dq\, \frac{1}{2} m^* q_0^2 d\omega_{\mathrm{LO}}(\epsilon_0 - \epsilon_\infty) \frac{q}{(q_0 + q)^2}$$

$$\times \left[\frac{1 + n_{\mathrm{B}}(\omega_{\mathrm{LO}}, T)}{-q^2 - 2m^*\omega_{\mathrm{LO}}} + \frac{n_{\mathrm{B}}(\omega_{\mathrm{LO}}, T)}{-q^2 + 2m^*\omega_{\mathrm{LO}}} \right]. \quad (3)$$

Here, m^* is the effective mass of the band, q_0 is a characteristic wave vector of the polaron in 2D materials [defined in Eq. (B6) and Refs. [51,52]], d is the effective thickness of the 2D material, ω_{LO} is the frequency of the longitudinal-optical phonon, and ϵ_∞ and ϵ_0 are the high-frequency and static relative permittivities, respectively. The details of the derivation are presented in Appendix B, where, very interestingly, we find that the dimensionality change from three to two significantly amplifies the mathematical intricacy involved in band renormalization.

C. Thermal expansion

In the context of experimentally probing the temperature dependent electron eigenenergy, a prevailing practice entails the execution of experiments under constant-pressure conditions. Therefore, it is necessary to also include the influence of thermal expansion on electron eigenenergies, which has been shown to make a comparable contribution to electron-phonon coupling in three-dimensional topological materials [21]. The temperature dependence of the electron eigenenergy induced by thermal expansion can be expressed as [42,43]:

$$\Delta E_{n\mathbf{k}}^{\mathrm{TE}}(T) = \int_0^T dT \left(\frac{\partial E_{n\mathbf{k}}}{\partial V} \right)_{T_0} \left(\frac{\partial V}{\partial T} \right)_{P_0}. \quad (4)$$

Here, $(\partial E_{n\mathbf{k}}/\partial V)_{T_0}$ represents the eigenenergy shift as the system volume changes at constant temperature T_0, and $(\partial V/\partial T)_{P_0}$ represents the volume change as the system temperature increases at constant pressure P_0.

D. First-principles implementation

To calculate band renormalization induced by short-wavelength phonons from first principles, we use Eq. (2) as our starting point. This choice [instead of Eq. (A6)] enables us to bypass the explicit calculation of the electron-phonon coupling matrix elements. The only terms that need to be numerically evaluated are the second-order derivatives of the band structure with respect to the displacement of each phonon. We implement this in the finite difference context using a three-point central formula:

$$\frac{\partial^2 E_{n\mathbf{k}}}{\partial \mu_{\nu\mathbf{q}}^2} \simeq \frac{E_{n\mathbf{k}}^{(+\delta\mu_{\nu\mathbf{q}})} + E_{n\mathbf{k}}^{(-\delta\mu_{\nu\mathbf{q}})} - 2E_{n\mathbf{k}}^{(0)}}{\delta\mu_{\nu\mathbf{q}}^2}, \quad (5)$$

where $E_{n\mathbf{k}}^{(+\delta\mu_{\nu\mathbf{q}})}$ represents the band structure calculated by incorporating a "frozen" phonon characterized by ν and $\mathbf{q}$ with a real displacement of $+\delta\mu_{\nu\mathbf{q}}$. In the case of degenerate band structures, the above second derivatives are averaged over all degenerate states. The BZ integration required by Eq. (2) is implemented by invoking the nonuniform $\mathbf{q}$-point sampling and nondiagonal supercell techniques [27,53] to ensure optimal efficiency.

To calculate band renormalization induced by long-wavelength phonons, we employ Cauchy's principal value integration to evaluate Eq. (3), circumventing the divergence arising from the singularity in the integrand when $-q^2 \pm 2m^*\omega_{\mathrm{LO}} = 0$. We note that Ref. [50] proposed the alternative approach of invoking the adiabatic approximation to merge the two singularities into one and shifting them off the real axis by an amount $i\eta$. Although we have also derived the counterpart for 2D materials following the same idea [as shown in Eq. (B7)], which might provide accurate results with a less dense $\mathbf{q}$-point grid when $i\eta$ is judiciously chosen, we opt not to adopt this approach in this work to avoid introducing the *ad hoc* parameter. All the parameters within Eq. (3) can be acquired through well-established first-principles methods. For instance, m^* can be determined by fitting the curvature of the band, while ϵ_∞ and ϵ_0 can be calculated by assessing the response of the system to an applied electric field.

To model thermal expansion from first principles through $(\partial V/\partial T)_{P_0}$ in Eq. (4), we use the quasiharmonic approximation to incorporate the volume dependence of phonon frequencies, such that the Helmholtz free energy of the vibrating lattice can be expressed as [54]:

$$F(V; T) = U(V; 0) + k_{\mathrm{B}} T \sum_{\nu\mathbf{q}} \ln \left[2 \sinh \left(\frac{\omega_{\nu\mathbf{q}}(V)}{2k_{\mathrm{B}} T} \right) \right], \quad (6)$$

where the first term is the potential energy for the static lattice and the second term is the vibrational contribution to the free energy. It is worth noting that the second term does not vanish at zero temperature; instead, it equals $\frac{1}{2} \sum_{\nu\mathbf{q}} \omega_{\nu\mathbf{q}}(V)$, which leads to the contribution from zero-point motion to thermal expansion. We further implement Eq. (6) by calculating the system of interest at a few volumes in the expansion and compression regime. At each volume, the static lattice potential energy $U(V; 0)$ can be obtained through a lattice-constrained geometry optimization, and the volume-dependent phonon frequency $\omega_{\nu\mathbf{q}}(V)$ can be obtained from the corresponding phonon calculations. By fitting the resulting Helmholtz free energy $F(V; T)$ with a polynomial function, we determine the volume corresponding to the minimum of $F(V; T)$ for a given temperature T, that is, the equilibrium volume at that temperature.

III. RESULTS AND DISCUSSION

A. Crystal structure

Monolayer TMDs have been confirmed to exhibit a series of stable and metastable phases, both in theory and experiments [55,56]. Of particular interest within this work is the 1T′ phase, which adopts a monoclinic structure characterized by the space group $P2_1/m$. Figure 1(a) visualizes the crystallographic structure from both top and side perspectives. The structure emerges as a spontaneous symmetry breaking from the 1T phase (with space group $P\bar{3}m1$) induced by the Peierls instability in which the M-M dimerization takes place, thereby eliminating the degeneracy of the states near the Fermi level and lowering the energy of the system. Despite the distortion of M atoms leading to the loss of certain symmetries, the 1T′ phase still possesses an inversion center, a mirror plane, and a
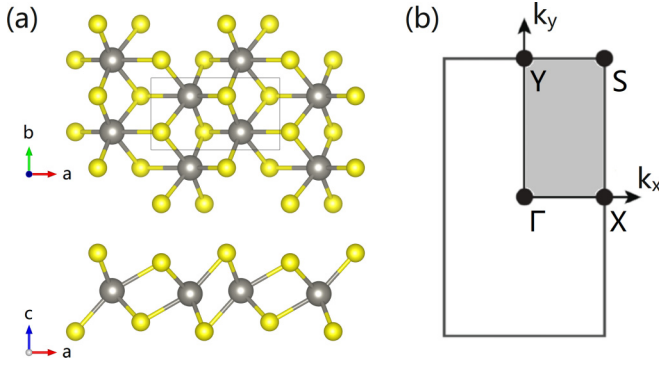
FIG. 1. (a) Crystal structure of 1T'-MX_2 and (b) its BZ. The gray and yellow balls represent the $M =$ W, Mo and $X =$ S, Se atoms respectively. The gray shaded area represents the irreducible Brillouin zone.

FIG. 2. Band structures of WS$_2$ with and without spin-orbit coupling (SOC) in the vicinity of the Γ point. The direct and indirect gaps are highlighted, where the former corresponds to the inverted band gap in the context of topological insulators.

twofold screw axis. Therefore, its irreducible Brillouin zone is a quarter of the whole Brillouin zone, as depicted in Fig. 1(b).

B. Computational details

We perform first-principles calculations at the density functional theory (DFT) level [57,58] with the Vienna *ab initio* simulation package (VASP) [59]. A vacuum layer with a thickness of 20 Å is used in the calculation to avoid periodic image interactions along the direction perpendicular to the plane. The interaction between ions and valence electrons is modeled with pseudopotentials based on the projector-augmented wave [60,61] method, where the valence electrons of the transition metals are $ns^2(n-1)d^5$ (where $n = 6$ for $M =$ W and $n = 5$ for $M =$ Mo) and the valence electrons of chalcogen are ns^2np^4 (where $n = 4$ for $X =$ Se and $n = 3$ for $X =$ S). The exchange-correlation functional is treated in the generalized gradient approximation parametrized by Perdew-Burke-Ernzerhof (PBE) [62] in most calculations. The Heyd-Scuseria-Ernzerhof (HSE) hybrid functional [63] is further used for WS$_2$ to reinforce the robustness of the findings on the band-gap size and temperature dependence. An energy cutoff of 500 eV for the plane-wave expansion and a Γ-centered **k**-point grid of size $5 \times 9 \times 1$ for Brillouin-zone integration are adopted in the calculations. The spin-orbit coupling is included in the calculations *via* a perturbation to the scalar relativistic Hamiltonian [64].

C. Electronic structures

It has been confirmed both in theory and experiments that the 1T'-MX_2 family are topological insulators [38,65–70]. In a broader context, the band structure of an inversion symmetric topological insulator is generally characterized by two band gaps, the indirect band gap, which corresponds to the minimum energy to excite an electron in the material bulk, and the direct band gap, where the band inversion takes place. Using WS$_2$ as a representative example, we show a typical band structure of a topological insulator in Fig. 2, where the band inversion induced by spin-orbit coupling occurs at the Γ point and leads to a double-well-shaped dispersion for the conduction band.
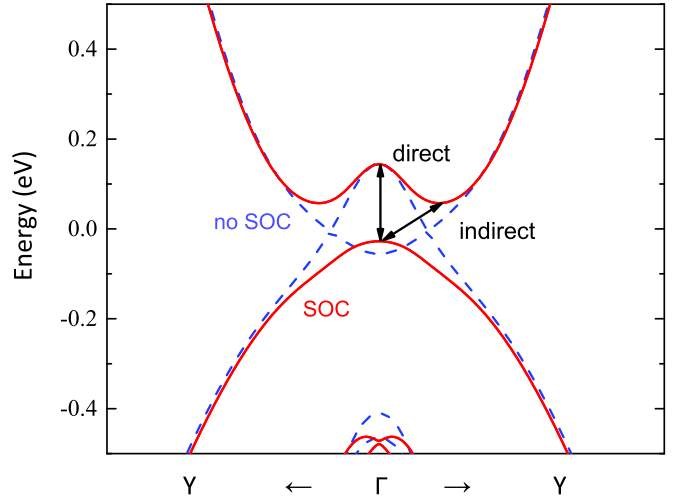
Following Ref. [38], we refer to the direct band gap at the Γ point as the inverted band gap, which reflects the band inversion strength of MX_2. Table I summarizes the values of the inverted band gaps for WS$_2$, WSe$_2$, MoS$_2$, and MoSe$_2$ at the static DFT level, where MoSe$_2$ exhibits the largest gap of 713 meV while WS$_2$ exhibits the smallest one of 183 meV. The results agree with previous first-principles studies [38,71].

The atomic-orbital projection analysis of the inverted band-gap point further reveals that the nontrivial topology of 1T'-MX_2 can be understood from the p-d band-inversion picture. We find that across all four compounds, the conduction-band inversion is primarily influenced by hybridization of metal d_{xz} and d_{yz} states. In the cases of MoS$_2$, WS$_2$, and WSe$_2$, their inverted conduction bands exhibit a similar pattern, predominantly stemming from contributions of the chalcogenide p_y orbitals. On the contrary, MoSe$_2$ distinguishes itself from them, displaying an inverted conduction band dominated by a mixture of Mo $d_{x^2-y^2}$ and d_{z^2} states. This state manifests a distinctly different orientation compared with the chalcogenide p_y orbitals, as shown in Figs. 3(a) and 3(d).

TABLE I. Static and renormalized band gap of WS$_2$, WSe$_2$, MoS$_2$, and MoSe$_2$ at $T = 0$ and 300 K. The total renormalization is equal to the sum of the renormalization induced by short- and long-wavelength phonons, $\Delta E^{S}(T)$ and $\Delta E^{L}(T)$, and the thermal expansion, $\Delta E^{TE}(T)$.

		WS$_2$	WSe$_2$	MoS$_2$	MoSe$_2$
	Static	183 meV	693 meV	531 meV	713 meV
ΔE^{S}	0 K	+17 meV	+5 meV	+4 meV	+8 meV
	300 K	+38 meV	+17 meV	+17 meV	+21 meV
ΔE^{L}	0 K	−8 meV	−5 meV	−2 meV	−5 meV
	300 K	−8 meV	−5 meV	−1 meV	−5 meV
ΔE^{TE}	0 K	−4 meV	−3 meV	−2 meV	−0.4 meV
	300 K	−17 meV	−16 meV	−13 meV	−1 meV
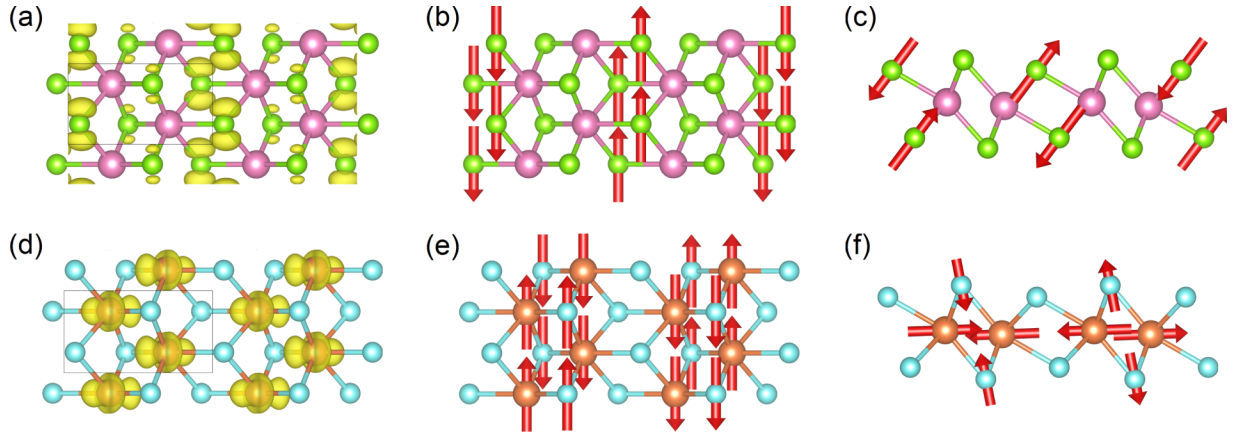
FIG. 3. Hole density of the state associated with the conduction-band extremum at the Γ point, alongside two vibration modes at the X point that exhibit strong coupling with it. Panels [(a)–(c)] correspond to MoS_2, WS_2, and WSe_2, while panels [(d)–(f)] correspond to $MoSe_2$. The red arrows indicate the vibration of the corresponding atoms.

D. Band-gap renormalization induced by electron-phonon coupling

To effectuate an electronic structure phase transition from a topologically nontrivial state (i.e., $1T'$-MX_2 at 0 K) to a topologically trivial state (if it exists), it is imperative for the inverted band gap at the Γ point to undergo closure. Therefore, in subsequent sections, we focus on the temperature effects on this inverted band gap. It is also worth noting that, as one of the most important manifestations of topology, the topologically protected metallic edge states are required to intersect at the Γ point because of time-reversal symmetry. The presence of a finite gap guarantees the insulating nature of the bulk and ensures that electronic transport can occur only through the topologically protected metallic edge states.

1. Short-wavelength phonon-induced band-gap renormalization

To obtain the phonon-induced band-gap renormalization, we first calculate the phonon spectra for the four compounds thereby determining the concrete form of real-valued operators $\partial/\partial\mu_{\nu q}$ for them. The obtained phonon spectra also allow us to theoretically confirm the dynamical stability of MX_2 at ambient pressure as there are no imaginary vibrational modes [see the Supplemental Material (SM) [72]].

Figure 4(a) shows the band-gap corrections ΔE^S as a function of temperature, while the specific values at both absolute zero and room temperature ($T = 300$ K) are presented in Table I. In contrast with the behavior typically observed in most semiconductors, where the band gap diminishes with rising temperature, $1T'$-MX_2 exhibits an opposite trend. Across the four TMDs investigated, regardless of the distinct chemical compositions, a consistent positive correlation between the band gap and temperature is evident. It is particularly pronounced at temperatures exceeding 100 K, showing an asymptotic linear dependence of the gap change with temperature. Below this temperature, only the low-frequency vibrational modes are excited and the phonon-induced band-gap renormalization remains relatively constant. For WSe_2, MoS_2, and $MoSe_2$, we find that they exhibit comparable band-gap corrections, around 20 meV at room temperature. In comparison, WS_2 manifests stronger electron-phonon

coupling, resulting in a band-gap renormalization of 38 meV, which is approximately double the values observed in the other three TMDs. This is a substantial correction, whose magnitude accounts for nearly 21% of the static band-gap size in WS_2.

To better understand the microscopic origin of the phonon-induced band-gap renormalization, we define the electron-phonon coupling strength in the temperature-dependent band structure context as

$$S^{\text{el-ph}}_{\nu q} = \frac{\partial^2 E_{\text{gap}}}{\partial\mu^2_{\nu q}}, \quad (7)$$

followed by the q-resolved electron-phonon coupling strength defined as

$$S^{\text{el-ph}}(q) = \sum_{\nu} S^{\text{el-ph}}_{\nu q}. \quad (8)$$

The bottom-left panels of Figs. 5(a)–5(d) depict the band structures for the four compounds along the high-symmetry path, from which it can be seen that their conduction-band minima are all located on the Γ-Y path. For WS_2 and $MoSe_2$, they exhibit a (negative) parabolic and quartic shaped valence band around the Γ point, respectively, while for WSe_2 and MoS_2, their valence band manifests a double-peak shape, resulting in the valence-band maximum shifting close to the conduction-band maximum on the Γ-Y path.

The top-left and -right panels of Figs. 5(a)–5(d) show the q-resolved electron-phonon coupling strength along the high-symmetry path and on the whole irreducible Brillouin zone, respectively. Within the upper half plane of the irreducible Brillouin zone, the electron-phonon coupling strength is nearly negligible. The principal contributions to the band renormalization are concentrated in proximity to the Γ and X points. Focusing on phonons at the X point, which corresponds to vibrational modes exhibiting a wavelength twice that of the original unit cell, we visualize in Figs. 3(b), 3(c) and 3(e), 3(f) the two modes that most strongly couple to the inverted band gap. Interestingly, these modes are highly localized along certain directions. For MoS_2, WS_2, and WSe_2, the dominant modes are very similar, all exclusively associated with chalcogenide atoms. One mode involves vibrations
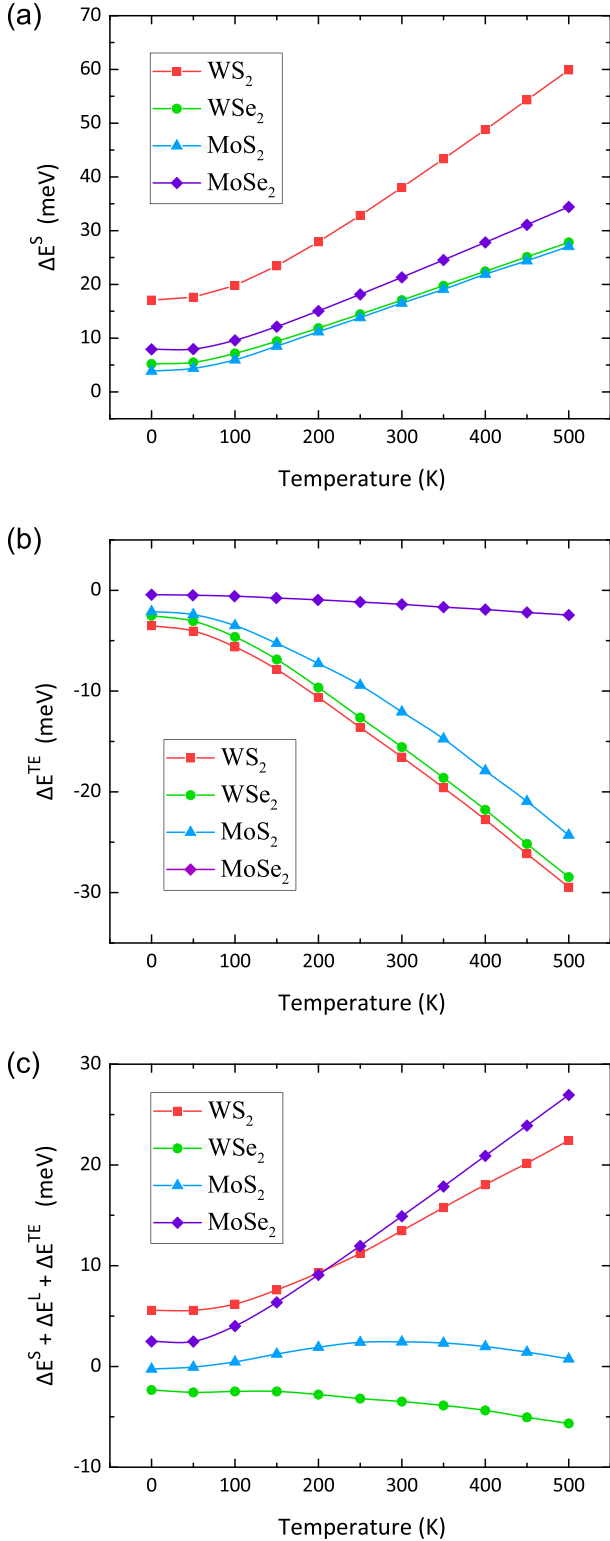
FIG. 4. Band-gap renormalization as a function of temperature for WS_2, WSe_2, MoS_2, and $MoSe_2$, where panels (a) and (b) show the contribution from short-wavelength phonons, $\Delta E^S(T)$, and thermal expansion, $\Delta E^{TE}(T)$, respectively, and panel (c) shows the overall effect including both electron-phonon coupling and thermal expansion.

along the **b** direction, inducing alternating shear deformation, while the other involves vibrations along the **a** and **c**

directions, asymmetrically stretching chalcogenide atoms. On the other hand, $MoSe_2$ shows a very different behavior, with the strong-coupling modes governed by atoms that remain static in the cases of MoS_2, WS_2, and WSe_2. This difference can be attributed to its distinct orbital component. As mentioned earlier, MoS_2, WS_2, and WSe_2 display a conduction band at the Γ point that mainly arises from chalcogenide p_y orbitals, whereas in $MoSe_2$, it originates from Mo $d_{x^2-y^2}$ and d_{z^2} orbitals. The modes we observe here can bring about a notable alteration in hole density, consequently renormalizing the inverted band gap.

A noteworthy finding is that within WS_2 alone, the inverted band gap exhibits a nonzero coupling to phonons at the Γ point, where the eighth phonon branch with a flat dispersion ($\omega_{vq} \approx 28$ meV) contributes nearly 73% electron-phonon coupling strength. This unique Γ point contribution drives a larger band-gap renormalization at room temperature in WS_2 compared with that of the other three compounds in the TMD family. Given the notorious band-gap problem of DFT [73], we have further employed the HSE hybrid functional to examine the lattice vibration modes that were observed to contribute significantly to the overall electron-phonon coupling strength at the PBE level. We find that the HSE functional "scales up" the static band gap and the electron-phonon coupling strength induced by the Γ and X phonons [74]. This observation is consistent with findings in conventional insulators; that is, extending calculations beyond semilocal DFT generally yields larger static band gaps and stronger electron-phonon coupling strength [75,76]. Since the overall electron-phonon coupling strength of WS_2 is dominated by the Γ- and X-phonons, we conclude that the HSE functional should not qualitatively change the finding based on the PBE functional, that is the temperature effect will increase the topological band gap in WS_2.

Finally, it is also worth noting that the electron-phonon coupling strength curves diverge at some **k** points. This divergence manifests as sharp peaks in the top-left panel of Figs. 5(a)–5(d) and visually evident red-blue dividing lines in the right panel. This feature arises from the double-peak and double-well characteristics of the band structure through the divergence of the electron-phonon coupling strength on the isoenergetic surface. This phenomenon can be rationalized using a perturbation theory framework and has been discussed in the case of bismuthene in Ref. [27]. The computational cost associated with treating the singularity in the electron-phonon coupling strength prevents the calculation of band-gap renormalization using the traditional uniform **q**-point grid. Therefore, here we have used a Farey grid of order 13, sampling 696 **q** points in the Brillouin zone, corresponding to 12 528 modes, to ensure convergence [77].

2. Long-wavelength phonon-induced band-gap renormalization

Given that monolayer 1T′-MX_2 possesses polar chemical bonds between M^{4+} and X^{2-} ions, it is worth examining the band renormalization contributed by long-wavelength phonons (i.e., Fröhlich coupling). Table II summarizes the essential quantities characterizing the Fröhlich interaction and the corresponding band renormalization values calculated at both 0 and 300 K. We find that the magnitude of the
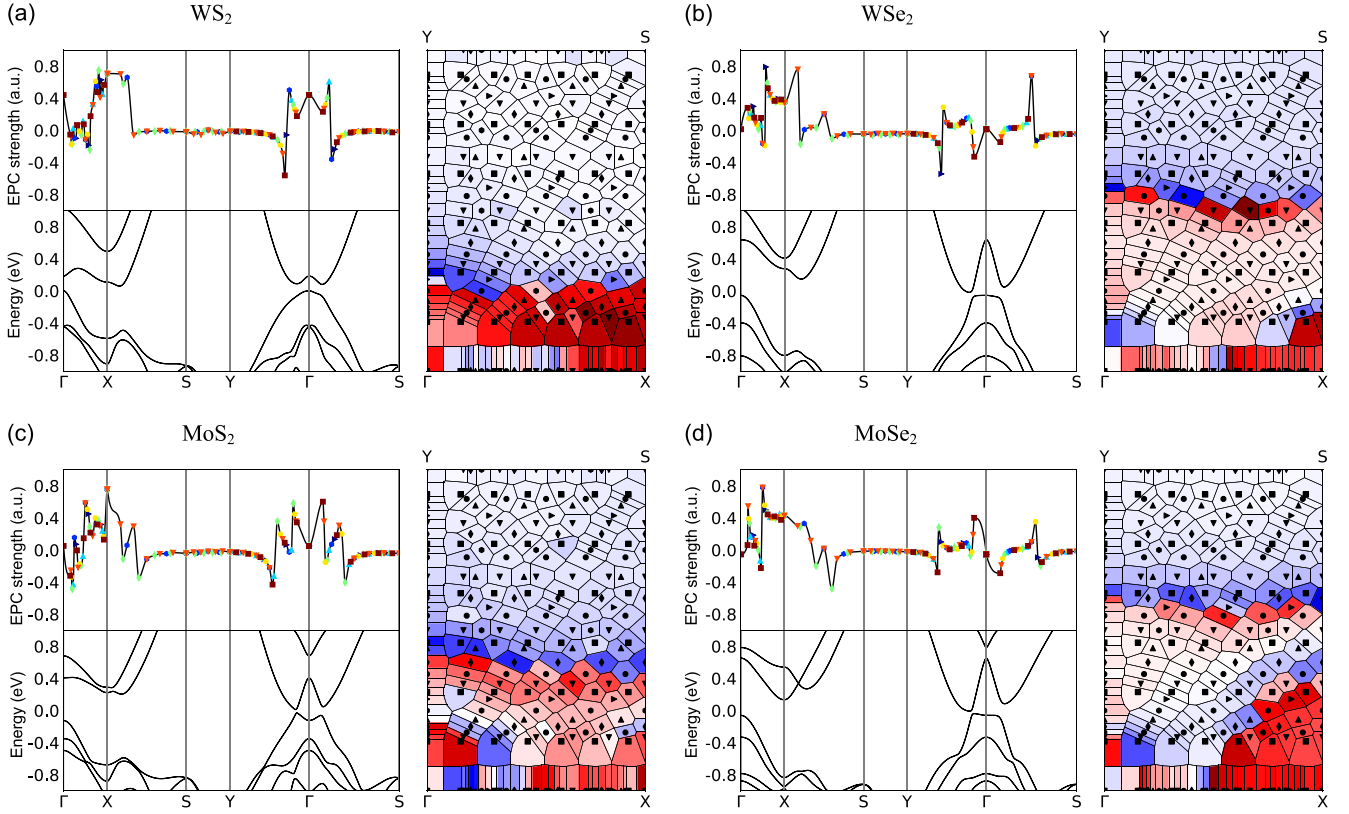
FIG. 5. q-resolved electron-phonon coupling strength (top-left panel) and band structure (bottom-left panel) for (a) WS$_2$, (b) WSe$_2$, (c) MoS$_2$, and (d) MoSe$_2$ along a high-symmetry path in the irreducible Brillouin zone. To calculate the band-gap renormalization, the irreducible Brillouin zone is sampled by a nonuniform Farey grid as shown in the right panel, where red and blue represent positive and negative electron-phonon coupling strengths, respectively, and the color depth represents the absolute value of the strength.

renormalization closely resembles that observed in the case induced by short-wavelength phonons at 0 K. Nevertheless, it is worth noting that the polaron-induced band renormalization exhibits minimal sensitivity to temperature fluctuations. This remarkable temperature independence can be attributed to the very small ionic contribution to the dielectric constant, $\epsilon_0 - \epsilon_\infty \approx 0.5$, across all four considered 2D TMDs. In

contrast, HgTe in CdTe/HgTe/CdTe quantum wells (as another realization of topological insulators) have $\epsilon_0 - \epsilon_\infty = 6$ [20], and typical ionic compounds have even larger values [78].

E. Thermal expansion

Now we consider the band gap renormalization induced by thermal expansion. Due to the 2D materials nature, all of 1T'-MX_2 have weak thermal expansion. The degree of thermal expansion is proportional to the atomic weight, where MoS$_2$ has the largest thermal expansion, but still does not exceed 0.7% [79].

Figure 4(b) shows the band-gap corrections ΔE^{TE} as a function of temperature, while the specific values at both absolute zero and room temperature ($T = 300$ K) are presented in Table I. Overall, the inverted band gaps of all four TMDs decrease as temperature increases. This behavior is expected to some extent, given that thermal expansion drives materials toward their atomic limits, while at the same time resulting in a topologically trivial band structure. However, it is worth noting that the band structures of WS$_2$, MoS$_2$, and WSe$_2$ exhibit significant sensitivity to thermal expansion, in contrast with MoSe$_2$, which shows minimal temperature dependence. This discrepancy may be attributed to the fact that the conduction-band extremum of WSe$_2$ at the Γ point predominantly arises from $d_{x^2-y^2}$ and d_{z^2} orbitals which

TABLE II. Material-specific parameters to evaluate the band-gap renormalization induced by long-wavelength phonons for WS$_2$, WSe$_2$, MoS$_2$, and MoSe$_2$. Except for ΔE^{L} which is in units of meV, the remaining quantities are reported in atomic units; that is, ω_{LO} in units of Hartree, m_c^* and m_v^* in units of the electron mass m_e, d in units of the Bohr radius a_0, and q_0 in units of $1/a_0$.

	WS$_2$	WSe$_2$	MoS$_2$	MoSe$_2$
ω_{LO}	1.26×10^{-3}	9.25×10^{-4}	1.26×10^{-3}	9.13×10^{-4}
ϵ_0	20.2	15.2	18.9	20.9
ϵ_∞	19.4	14.8	18.6	20.5
m_c^*	-0.553	-0.099	-0.127	-0.076
m_v^*	-0.622	-2.034	0.798	27.781
d	11.5	12.2	11.5	12.2
q_0	8.97×10^{-3}	1.11×10^{-2}	9.36×10^{-3}	18.0×10^{-3}
ΔE^{L}(0K)	-8 meV	-5 meV	-2 meV	-5 meV
ΔE^{L}(300K)	-8 meV	-5 meV	-1 meV	-5 meV

exhibit greater localization. The localized nature of these orbitals results in smaller changes in the band gap of $MoSe_2$ when the lattice parameter changes due to thermal expansion.

Finally, it is worth highlighting that our quasiharmonic approximation model is exclusively focused on isotropic thermal expansion. Nevertheless, the established dependence of the band gap in MX_2 under anisotropic strain [15] implies that the inclusion of anisotropic thermal expansion would not qualitatively alter our conclusions.

F. Overall temperature dependence

In the end, we investigate the overall temperature dependence of the inverted band gap. Figure 4(c) shows total band-gap corrections as a function of temperature, taking into account the contributions from both electron-phonon coupling and thermal expansion. We find that although WS_2 exhibits the strongest electron-phonon coupling, this effect is tempered by substantial thermal expansion, thereby attenuating the band-gap renormalization to some extent. On the other hand, $MoSe_2$, despite its less prominent electron-phonon coupling, stands out with the most substantial renormalized band gap when the temperature exceeds 200 K, thanks to its very weak thermal expansion. The corresponding band-gap renormalization reaches around 15 meV at room temperature. In comparison, MoS_2 and WSe_2 show a less pronounced temperature dependence. The band-gap renormalization of MoS_2 reaches a negligible maximum of 3 meV at 300 K. Beyond this point, thermal expansion gains prominence, resulting in a reduction in the band gap. As for WSe_2, the electron-phonon coupling is outweighed by thermal expansion at all temperatures, leading to a monotonic decrease in the band gap with increasing temperature.

IV. INVERSE VARSHNI EFFECT DRIVEN BY BAND INVERSION

Our observations in the four monolayer TMDs show that there seems to be no general trend for the sign of the correction to the band gap in topological insulators: temperature can either promote or suppress the topological phase. This complexity arises from the multiple ways in which temperature can exert its effects, and the competition between these effects is highly contingent upon the very details of the system.

Nevertheless, valuable insights can be gleaned from a very simple model in which electron-phonon coupling itself is indeed conducive to promoting the topological phase when significant band inversion occurs. To illustrate this, let us first consider a normal insulator characterized by parabolic valence and conduction bands at the Γ point where $m_c > 0$ and $m_v < 0$. The band extrema are simply coupled to all other states by a dispersionless phonon with frequency ω_0. Assuming that the Debye-Waller term is considerably smaller than the Fan-Migdal term (see the definitions in Appendix A), the predominant correction to the band gap occurs near the Γ point where $E_{n\Gamma}^{(0)} - E_{m\Gamma+q}^{(0)} = \pm q^2/2|m^*|$ [see Eq. (A6)]. The plus (minus) sign is for the valence (conduction) band, and m^* describes the effective masses. As a result, the temperature

dependence of the band gap takes the form

$$
E_{\text{gap}}(T) = \begin{cases} \dfrac{-Ce^{\omega_0/(k_B T)}}{e^{\omega_0/(k_B T)}-1} & \text{for 3D} \\[2ex] \dfrac{A-Be^{\omega_0/(k_B T)}}{e^{\omega_0/(k_B T)}-1} & \text{for 2D}, \end{cases} \tag{9}
$$

where $C > 0$ and $B > A$. The negative sign arises from the opposite curvatures of the valence and conduction bands. This simplified model affords insights into the so-called "Varshni effect" [80] observed in semiconductor physics: the reduction in the energy gap of semiconductors as a function of temperature, a phenomenon observed in the vast majority of insulators.

Interestingly, when applying this same simplified model to an insulator with an inverted band gap, characterized by $m_c < 0$ and $m_v > 0$, we find

$$
E_{\text{gap}}(T) = \begin{cases} \dfrac{C}{e^{\omega_0/(k_B T)}-1} & \text{for 3D} \\[2ex] \dfrac{B-Ae^{\omega_0/(k_B T)}}{e^{\omega_0/(k_B T)}-1} & \text{for 2D}, \end{cases} \tag{10}
$$

from which one can anticipate an "inverse Varshni effect." This is particularly relevant because topological insulators often exhibit band inversion with the above band curvature characteristics.

The same argument also holds to the band renormalization induced by Fröhlich coupling [see Eq. (B8)], where the sign of the effective mass of the electrons and holes determines the sign of the renormalization. In a more general manner, one can interpret $g_{mn\nu}(\boldsymbol{k}, \boldsymbol{q})$ in Eq. (A6) as $g_{mn\nu}(\boldsymbol{k}, \boldsymbol{q}) = g_{mn\nu}^{S}(\boldsymbol{k}, \boldsymbol{q}) + g_{mn\nu}^{L}(\boldsymbol{k}, \boldsymbol{q})$, encompassing both short- and long-wavelength contributions to the electron-phonon coupling matrix element [49]. Thus, we conclude that electron-phonon coupling should broadly promote the topology of systems with a significant band inversion feature. Following the above insight, we have applied the model in Eq. (10) to fit the band-gap renormalization induced by electron-phonon coupling in $1T'$-MX_2. The model is found to be able to accurately reproduce the results from first principles [81].

Overall, our simple model suggests that the inverse Varshni effect should be more prevalent in topological insulators than in normal insulators. We also note that Garate and Saha reached the same conclusion by considering the renormalization of Dirac mass (instead of the band gap) at finite temperatures [19,20], while Antonius and Louie further provided a symmetry argument making the picture more nuanced [22].

V. TEMPERATURE-TUNABLE TOPOLOGICAL STATES IN $1T'$-WS_2

The strong electron-phonon coupling in $1T'$-WS_2 which promotes topology offers a facile mechanism to control the topological order by temperature. To realize this, we consider applying positive biaxial strain to first drive the system to a normal insulator with an uninverted gap. Without considering electron-phonon coupling, we find that the inverted band gap first decreases to zero at strain of 2.2% and then reopens as the strain increases. By explicitly calculating the Z_2 topological invariant, we confirm that this gap-closing indeed induces a topological phase transition associated with the destruction of the edge states.
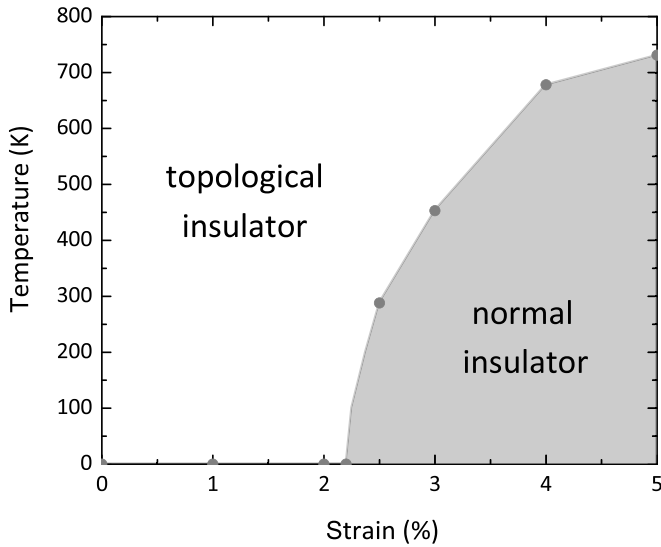
FIG. 6. Temperature-strain phase diagram of WS$_2$.

Figure 6 shows the temperature-strain phase diagram of WS$_2$. In the range of strain up to 5%, we consistently observe that electron-phonon coupling drives the electronic structure of 1T′-WS$_2$ toward its topologically nontrivial region. This agrees with the previous theoretical model introduced in Sec. IV. In particular, we find that at a strain of approximately 2.5%, elevating the temperature to 300 K drives a phase transition taking the system from the topologically trivial state imposed by strain to the topologically nontrivial phase. Therefore, temperature has an impact on the critical point of the topological phase transition engineered by strain. For example, referring to Fig. 6, at zero temperature the critical strain is found to be 2.2%, while at room temperature $T = 300$ K, the critical strain increases to 2.5%. As the first example of temperature promoted topological insulating phases, this temperature-strain tunable state holds promise for tailoring device functionalities.

VI. CONCLUSION

In summary, through first principles calculations, we have elucidated the role of three critical temperature-related factors: electron-phonon coupling, Fröhlich coupling, and thermal expansion, providing a comprehensive examination of the intricate temperature effects in 1T′-MX_2 monolayers.

Our findings demonstrate that within 1T′-MX_2 monolayers electron-phonon coupling generally promotes the topology of the electronic structures. However, the counteracting influence of thermal expansion should not be overlooked because it generally diminishes the topological attributes and holds the potential to reverse the temperature dependence of the band gap in some cases. This finding also sheds light on using a substrate that can suppress thermal expansion to achieve better thermal robustness of 2D topological insulators.

Furthermore, our investigation into Fröhlich coupling in 2D materials has revealed its relatively modest temperature dependence within 1T′-MX_2 monolayers due to the small ionic contribution to the dielectric constant. However, the formulation we have found is universal for all 2D

materials, which can be useful for understanding the strong band renormalization in the 2D materials that exhibit large ionic contribution to the dielectric constant.

In the context of material science, one of the outcomes of our study is the identification of MoSe$_2$ as a promising candidate for room-temperature applications. It exhibits remarkable resilience against thermal expansion, making it a robust choice for electronic devices operating at higher temperatures. Additionally, WS$_2$ displays tunable topological behavior under the combined influence of strain and temperature, opening up possibilities for tailored device functionalities. Both materials stand out as novel examples of temperature promoted topological insulators.

Overall, our work advances the fundamental understanding of temperature effects in 1T′-MX_2 monolayers, paving the way for the applications of 2D topological insulators.

APPENDIX A: REAL-VALUED PHONON DISPLACEMENT OPERATOR

Following the procedure that has been described in many textbooks of lattice dynamics [82,83], we define the normal coordinates $u_{v q}$ from the atomic displacements $l_{p \alpha j}$ for the phonon system as follows:

$$u_{v q} = \frac{1}{\sqrt{N_\mathrm{p}}} \sum_{p \alpha j} \sqrt{m_\alpha} l_{p \alpha j} e^{-i q \cdot \mathcal{R}_{p \alpha}} \xi^*_{v q \alpha j}, \qquad \text{(A1)}$$

or inversely,

$$l_{p \alpha j} = \frac{1}{\sqrt{N_\mathrm{p}}} \sum_{v q} \frac{1}{\sqrt{m_\alpha}} u_{v q} e^{i q \cdot \mathcal{R}_{p \alpha}} \xi_{v q \alpha j}, \qquad \text{(A2)}$$

where p and α run over all primitive cells of the crystal and the ions in the cell, respectively, j denotes the Cartesian components, m_α is the mass of ion α, N_p is the number of primitive cells in the crystal, and $\xi_{v q \alpha j}$ is the eigenvector of the dynamical matrix of the system.

It is worth noting that $u_{\nu q}$ is generally complex (because $\xi_{\nu q \alpha j}$ is complex), but one can construct a set of real-valued phonon displacement from $u_{\nu q}$ by partitioning the phonon BZ into three parts:

$$\mathrm{BZ} = \mathrm{BZ}_0 \cup \mathrm{BZ}_{+1} \cup \mathrm{BZ}_{-1}. \tag{A3}$$

Here $\mathrm{BZ}_0 = \{q \notin \mathrm{BZ}_{\pm 1} | q = -q \bmod \mathcal{G}\}$ represents a set of discrete q points invariant under inversion modulo a reciprocal-lattice vector (i.e.the center of the Brillouin zone, the centers of its faces, and the corners), and $\mathrm{BZ}_{\pm 1} = \{q \notin \mathrm{BZ}_0 | -q \in \mathrm{BZ}_{\mp 1}\}$ are mutually inversion-symmetric images, each including all the q-points that are not inversion partners. On this partitioning, we define the real phonon displacement

$$\mu_{\nu q} = \begin{cases} u_{\nu q} & \text{for } q \in \mathrm{BZ}_0 \\ \frac{1}{\sqrt{2}}(u_{\nu q} + u_{\nu -q}) & \text{for } q \in \mathrm{BZ}_{+1} \\ \frac{i}{\sqrt{2}}(u_{\nu q} - u_{\nu -q}) & \text{for } q \in \mathrm{BZ}_{-1}, \end{cases} \tag{A4}$$

or inversely,

$$u_{\nu q} = \begin{cases} \mu_{\nu q} & \text{for } q \in \mathrm{BZ}_0 \\ \frac{1}{\sqrt{2}}(\mu_{\nu q} + i\mu_{\nu -q}) & \text{for } q \in \mathrm{BZ}_{+1} \\ \frac{1}{\sqrt{2}}(\mu_{\nu -q} - i\mu_{\nu q}) & \text{for } q \in \mathrm{BZ}_{-1}. \end{cases} \tag{A5}$$

From Eq. (A4), one can naturally define a real-value phonon differential operator $\partial / \partial \mu_{\nu q}$, which has been used in the main text to reformulate AHC theory.

We note that one widely used formulation of $E_{nk}(T)$ is given as follows [84]:[1]

$$\begin{aligned} E_{nk}(T) = E_{nk}^{(0)} &+ \frac{1}{N_\mathrm{p}} \sum_{\nu q} \left[\sum_m \frac{|g_{mn\nu}(k,q)|^2}{E_{nk}^{(0)} - E_{mk+q}^{(0)}} + g_{nn\nu\nu}^{\mathrm{DW}}(k,q,-q) \right] \\ &\times \left[1 + 2n_\mathrm{B}(\omega_{\nu q}, T) \right], \end{aligned} \tag{A6}$$

where

$$g_{mn\nu}(k,q) = \langle \varphi_{mk+q} | \partial_{\nu q} \mathcal{V}_{\mathrm{el}} | \varphi_{nk} \rangle \tag{A7}$$

is referred to as the Fan-Migdal electron-phonon coupling matrix, $\mathcal{V}_{\mathrm{el}}$ is the potential experienced by the electrons in crystals, and $g_{nn\nu\nu}^{\mathrm{DW}}(k,q,-q)$ is a particular case of the Debye-Waller electron-phonon matrix,

$$g_{mn\nu\nu'}^{\mathrm{DW}}(k,q,q') = \tfrac{1}{2} \langle \varphi_{mk+q+q'} | \partial_{\nu q} \partial_{\nu' q'} \mathcal{H}_{\mathrm{el}} | \varphi_{nk} \rangle. \tag{A8}$$

Here the (complex) phonon differential operator $\partial_{\nu q}$ is formulated as [46,85]

$$\partial_{\nu q} \equiv \frac{1}{\sqrt{2\omega_{\nu q}}} \sum_{p\alpha j} \frac{1}{\sqrt{m_\alpha}} e^{iq \cdot \mathcal{R}_{p\alpha}} \xi_{\nu q\alpha j} \frac{\partial}{\partial l_{p\alpha j}}. \tag{A9}$$

We show that Eqs. (2) and (A6) are equivalent. First, the second-derivative term in Eq. (2) can be split into two terms

---

[1] The sum excludes $q = 0$ for the first term in $\sum_{\nu q}[\ldots]$ when $m = n$.

by invoking the Hellmann-Feynman theorem [86], i.e.,

$$\begin{aligned} \frac{\partial^2 E_{nk}}{\partial \mu_{\nu q}^2} = &\left\langle \varphi_{nk} \left| \frac{\partial^2 \mathcal{H}_{\mathrm{el}}}{\partial \mu_{\nu q}^2} \right| \varphi_{nk} \right\rangle \\ &+ \left\langle \varphi_{nk} \left| \frac{\partial \mathcal{H}_{\mathrm{el}}}{\partial \mu_{\nu q}} \right| \frac{\partial \varphi_{nk}}{\partial \mu_{\nu q}} \right\rangle + \left\langle \frac{\partial \varphi_{nk}}{\partial \mu_{\nu q}} \left| \frac{\partial \mathcal{H}_{\mathrm{el}}}{\partial \mu_{\nu q}} \right| \varphi_{nk} \right\rangle, \end{aligned} \tag{A10}$$

where the derivative of the state can be resolved by an unperturbed complete basis set $\{|\varphi_{nk}\rangle\}$ according to perturbation theory [87] as follows:

$$\left| \frac{\partial \varphi_{nk}}{\partial \mu_{\nu q}} \right\rangle = \sum_{\substack{(m,k') \\ \neq (n,k)}} |\varphi_{mk'}\rangle \frac{\langle \varphi_{mk'} | \frac{\partial \mathcal{H}_{\mathrm{el}}}{\partial \mu_{\nu q}} | \varphi_{nk} \rangle}{E_{nk}^{(0)} - E_{mk'}^{(0)}}. \tag{A11}$$

Second, using the chain rule, one can find that the complex phonon differential operator is related to our real-displacement phonon differential operator by the relation

$$\frac{\partial}{\partial \mu_{\nu q}} = \begin{cases} \sqrt{\frac{2\omega_{\nu q}}{N_\mathrm{p}}} \partial_{\nu q} & \text{for } q \in \mathrm{BZ}_0 \\ 2\sqrt{\frac{\omega_{\nu q}}{N_\mathrm{p}}} \partial_{\nu q} & \text{for } q \in \mathrm{BZ}_{+1} \\ 0 & \text{for } q \in \mathrm{BZ}_{-1}, \end{cases} \tag{A12}$$

and thus

$$\lim_{N_\mathrm{p} \to \infty} \sum_{\nu q} \frac{\partial}{\partial \mu_{\nu q}} = \lim_{N_\mathrm{p} \to \infty} \sum_{\nu q} \sqrt{\frac{\omega_{\nu q}}{N_\mathrm{p}}} \partial_{\nu q}. \tag{A13}$$

Substituting Eqs. (A10)–(A13) into Eq. (2) yields exactly Eq. (A6), so the equivalence is proved. We also note that Refs. [44,88] derived another formulation of $E_{nk}(T)$ using a generalized Janak's theorem. Similarly, one can also show that their result

$$E_{nk}(T) = E_{nk}^{(0)} + \frac{1}{2N_\mathrm{p}} \sum_{\nu q} \frac{\partial E_{nk}}{\partial n_\mathrm{B}} [1 + 2n_\mathrm{B}(\omega_{\nu q}, T)], \tag{A14}$$

with

$$\begin{aligned} \frac{\partial E_{nk}}{\partial n_\mathrm{B}} = &\frac{1}{2\omega_{\nu q}} \sum_{p\alpha j} \sum_{p'\alpha' j'} \frac{\partial^2 E_{nk}}{\partial l_{p\alpha j} \partial l_{p'\alpha' j'}} e^{-iq \cdot (\mathcal{R}_{p\alpha} - \mathcal{R}_{p'\alpha'})} \\ &\times \frac{\xi_{\nu q\alpha j}}{\sqrt{m_\alpha}} \frac{\xi_{\nu q\alpha' j'}^*}{\sqrt{m_{\alpha'}}}, \end{aligned} \tag{A15}$$

is equivalent to ours.

It is worth noting that the Debye-Waller term involving second-order electron-phonon matrix elements is very challenging to calculate in the density functional perturbation theory framework, therefore one has to invoke the rigid-ion approximation to rewrite it as the product of first-order electron-phonon matrix elements. However, it can be easily included in the finite difference framework as used in this work.

APPENDIX B: FRÖHLICH COUPLING IN TWO DIMENSIONS

For polar insulators, it has been known that the presence of Fröhlich coupling can play a role in the additional renormalization of the band structure. Here we provide a derivation

for this. We start by considering a hole at the Γ point of the conduction band $E_{mq}^{(0)}$ interacting with a single dispersionless polar longitudinal-optical phonon of frequency ω_{LO}. At a finite temperature T, the self-energy for the hole polaron reads

$$
\Sigma^{\mathrm{Fr}}(\omega) = \int \frac{d\boldsymbol{q}}{\Omega_{\mathrm{BZ}}} |g(\boldsymbol{q})|^2 \left[\frac{1 - n_{\mathrm{F}}\big(E_{cq}^{(0)}, T\big) + n_{\mathrm{B}}(\omega_{\mathrm{LO}}, T)}{\omega - E_{cq}^{(0)} - \omega_{\mathrm{LO}} + i\eta} \right.
$$
$$
\left. + \frac{n_{\mathrm{F}}\big(E_{cq}^{(0)}, T\big) + n_{\mathrm{B}}(\omega_{\mathrm{LO}}, T)}{\omega - E_{cq}^{(0)} + \omega_{\mathrm{LO}} + i\eta} \right], \tag{B1}
$$

where Ω_{BZ} is the volume of the Brillouin zone, η is a positive infinitesimal, and $n_{\mathrm{F}}(E_{cq}^{(0)}, T) = [\exp(E_{cq}^{(0)}/k_{\mathrm{B}}T) + 1]^{-1}$ is the Fermi-Dirac factor. The band renormalization arising from $\Sigma^{\mathrm{Fr}}(\omega)$ can be obtained from the standard prescription of many-body perturbation theory:

$$
E_{c\Gamma}(T) = E_{c\Gamma}^{(0)} + \int \frac{d\boldsymbol{q}}{\Omega_{\mathrm{BZ}}} |g(\boldsymbol{q})|^2
$$
$$
\times \left[\frac{1 + n_{\mathrm{B}}(\omega_{\mathrm{LO}}, T)}{-|\boldsymbol{q}|^2 - q_{\mathrm{LO}}^2} + \frac{n_{\mathrm{B}}(\omega_{\mathrm{LO}}, T)}{-|\boldsymbol{q}|^2 + q_{\mathrm{LO}}^2} \right], \tag{B2}
$$

where we have made the following approximations: (i) the conduction band near the Γ point is isotropic and parabolic, i.e., $E_{cq}^{(0)} = \boldsymbol{q}^2/2m^*$, where m^* is the effective mass. (2) $k_{\mathrm{B}}T \ll E_{cq}^{(0)}$ thereby $n_{\mathrm{F}}(E_{cq}^{(0)}, T) = 0$ for all conduction states near the Γ point. (iii) $\Sigma^{\mathrm{Fr}}(\omega)$ is purely real-valued, i.e., $i\eta = 0$. In addition, we have defined the effective longitudinal optical wave vector $q_{\mathrm{LO}}^2 = 2m^*\omega_{\mathrm{LO}}$.

We first examine Eq. (B2) in the 3D case, in which the Fröhlich electron-phonon coupling matrix has a long-known expression given by [47–49]

$$
|g(\boldsymbol{q})|^2 = \frac{2\pi}{V_{\mathrm{cell}}} \omega_{\mathrm{LO}} \left(\frac{1}{\epsilon_\infty} - \frac{1}{\epsilon_0} \right) \frac{1}{|\boldsymbol{q}|^2}, \tag{B3}
$$

where V_{cell} is the volume of the primitive cell, ϵ_∞ and ϵ_0 are the high-frequency and static relative permittivity, respectively. By substituting Eq. (B3) into Eq. (B2) and approximating the Brillouin-zone integration as $\int d\boldsymbol{q} = \int_0^{q_{\mathrm{BZ}}} dq\, 4\pi q^2 = \Omega_{\mathrm{BZ}}$, we arrive at

$$
E_{c\Gamma}(T) = E_{c\Gamma}^{(0)} + \int_0^{q_{\mathrm{BZ}}} dq\, \frac{2}{\pi} m^*\omega_{\mathrm{LO}} \left(\frac{1}{\epsilon_\infty} - \frac{1}{\epsilon_0} \right)
$$
$$
\times \left[\frac{1 + n_{\mathrm{B}}(\omega_{\mathrm{LO}}, T)}{-q^2 - q_{\mathrm{LO}}^2} + \frac{n_{\mathrm{B}}(\omega_{\mathrm{LO}}, T)}{-q^2 + q_{\mathrm{LO}}^2} \right]
$$

$$
= E_{c\Gamma}^{(0)} + \frac{2}{\pi} m^*\omega_{\mathrm{LO}} \left(\frac{1}{\epsilon_\infty} - \frac{1}{\epsilon_0} \right)
$$
$$
\times \left[-\frac{1 + n_{\mathrm{B}}(\omega_{\mathrm{LO}}, T)}{q_{\mathrm{LO}}} \tan^{-1}\left(\frac{q_{\mathrm{BZ}}}{q_{\mathrm{LO}}} \right) \right.
$$
$$
\left. + \frac{n_{\mathrm{B}}(\omega_{\mathrm{LO}}, T)}{q_{\mathrm{LO}}} \tanh^{-1}\left(\frac{q_{\mathrm{LO}}}{q_{\mathrm{BZ}}} \right) \right]. \tag{B4}
$$

A frequently employed treatment to further simplify the above expression is to set $q_{\mathrm{BZ}} \to \infty$, typically leading to an error in the value of the integral of the order of 10% [89]. Following this treatment and considering $T = 0$, we obtain the Fröhlich zero-point band renormalization $\Delta E_{c\Gamma}^{\mathrm{Fr}}(0) = -\frac{m^*\omega_{\mathrm{LO}}}{q_{\mathrm{LO}}}(\frac{1}{\epsilon_\infty} - \frac{1}{\epsilon_0}) = -\alpha\omega_{\mathrm{LO}}$, where $\alpha = \frac{m^*}{q_{\mathrm{LO}}}(\frac{1}{\epsilon_\infty} - \frac{1}{\epsilon_0})$ is the dimensionless polaron constant. This outcome aligns precisely with the previously known conclusion about polarons [89].

Now, we move to the 2D case. It is worth noting that, unlike the 3D case where the volume element (i.e., spherical shell) $4\pi q^2 dq$ can alleviate the singularity of the integral at $q = 0$, in the 2D case the area element (i.e. an annulus) $2\pi q dq$ does not possess the same capability. If one insists on using the Fröhlich electron-phonon coupling matrix given in Eq. (B3) which is proportional to $|\boldsymbol{q}|^{-2}$, the 2D integral involved in Eq. (B2) will invariably diverge. The primary cause for this divergence can be attributed to the oversimplification of a 2D material, treated merely as a mere sheet lacking thickness, in the modeling of polarons. This has been clearly described in Ref. [52].

To avoid the divergence mentioned above, we employ the recently proposed 2D Fröhlich electron-phonon coupling matrix [51]

$$
|g(\boldsymbol{q})|^2 = \left[\frac{\pi d}{2A_{\mathrm{cell}}} \omega_{\mathrm{LO}}(\epsilon_0 - \epsilon_\infty) \right] \frac{q_0^2}{(|\boldsymbol{q}| + q_0)^2} \tag{B5}
$$

to derive the Fröhlich band renormalization for 2D materials, where A_{cell} is the area of the primitive cell, d is the effective thickness of the 2D material, and q_0 is defined as

$$
q_0 = \frac{4\epsilon_\infty}{(2\epsilon_\infty^2 - 1)d}. \tag{B6}
$$

Again, by substituting Eq. (B5) into Eq. (B2) and approximating the Brillouin zone integration as $\int d\boldsymbol{q} = \int_0^\infty dq\, 2\pi q$, we arrive at

$$
E_{c\Gamma}(T) = E_{c\Gamma}^{(0)} + \int_0^\infty dq\, \frac{1}{2} m^* q_0^2 d\omega_{\mathrm{LO}}(\epsilon_0 - \epsilon_\infty) \frac{q}{(q_0 + q)^2} \left[\frac{1 + n_{\mathrm{B}}(\omega_{\mathrm{LO}}, T)}{-q^2 - q_{\mathrm{LO}}^2} + \frac{n_{\mathrm{B}}(\omega_{\mathrm{LO}}, T)}{-q^2 + q_{\mathrm{LO}}^2} \right]
$$
$$
= E_{c\Gamma}^{(0)} + \frac{1}{2} m^* q_0^2 d\omega_{\mathrm{LO}}(\epsilon_0 - \epsilon_\infty) \left\{ -\frac{q_{\mathrm{LO}}^2 - q_0^2[2n_{\mathrm{B}}(\omega_{\mathrm{LO}}, T) + 1]}{q_0^4 - q_{\mathrm{LO}}^4} - \frac{\pi q_0 q_{\mathrm{LO}}[n_{\mathrm{B}}(\omega_{\mathrm{LO}}, T) + 1]}{\left(q_0^2 + q_{\mathrm{LO}}^2 \right)^2} \right.
$$
$$
\left. -\frac{\big[2q_0^2(q_0^4 + 3q_{\mathrm{LO}}^4)n_{\mathrm{B}}(\omega_{\mathrm{LO}}, T) + \big(q_0^2 - q_{\mathrm{LO}}^2\big)^3 \big][\ln(q_0) - \ln(q_{\mathrm{LO}})]}{\big(q_0^4 - q_{\mathrm{LO}}^4 \big)^2} \right\}. \tag{B7}
$$

In a similar manner, one can find the expression for the correction to the valence band $E_{v\Gamma}(T)$.

Invoking the adiabatic approximation by replacing the term in the bracket of Eq. (3) by $[2n_B(\omega_{LO}, T) + 1]/(-q^2 + i2m^*\eta)$ and then taking the real part [50], we obtain

$$
\begin{aligned}
E_{c\Gamma}(T) &= E_{c\Gamma}^{(0)} + \mathrm{Re}\left\{ \int_0^\infty dq\, \frac{1}{2} m^* q_0^2 d\omega_{LO}(\epsilon_0 - \epsilon_\infty) \frac{q}{(q_0 + q)^2} \frac{2n_B(\omega_{LO}, T) + 1}{-q^2 + i2m^*\eta} \right\} \\
&= E_{c\Gamma}^{(0)} + \frac{1}{8} m^* q_0^2 d\omega_{LO}(\epsilon_0 - \epsilon_\infty)[2n_B(\omega_{LO}, T) + 1] \\
&\quad \times \mathrm{Re}\left\{ -\frac{2(\pi - 4i)m^*\eta - (4 - 4i)\pi q_0 \sqrt{m^*\eta}}{(2m^*\eta + iq_0^2)^2} - \frac{(4 - i\pi)q_0^2 + 2(q_0^2 + i2m^*\eta)[\ln(2m^*\eta/q_0^2)]}{(2m^*\eta + iq_0^2)^2} \right\}.
\end{aligned}
\tag{B8}
$$

It is worth noting that the small imaginary component $i\eta$ introduced here is *ad hoc* rather than *ab initio*. The physical meaning of η can be inferred as a finite lifetime for the unoccupied electronic states due to thermal effects. In principle, in more accurate approaches the η should be replaced by the finite physical linewidth of electrons. As already pointed out by Ref. [88], decreasing η does not lead to convergence for polar materials. One has to treat this with caution in band renormalization calculations.

[1] C. L. Kane and E. J. Mele, Z_2 topological order and the quantum spin Hall effect, Phys. Rev. Lett. **95**, 146802 (2005).

[2] C. L. Kane and E. J. Mele, Quantum spin Hall effect in graphene, Phys. Rev. Lett. **95**, 226801 (2005).

[3] B. A. Bernevig, T. L. Hughes, and S. Zhang, Quantum spin Hall effect and topological phase transition in HgTe quantum wells, Science **314**, 1757 (2006).

[4] M. Z. Hasan and C. L. Kane, Colloquium: Topological insulators, Rev. Mod. Phys. **82**, 3045 (2010).

[5] X.-L. Qi and S.-C. Zhang, Topological insulators and superconductors, Rev. Mod. Phys. **83**, 1057 (2011).

[6] A. Bansil, H. Lin, and T. Das, Colloquium: Topological band theory, Rev. Mod. Phys. **88**, 021004 (2016).

[7] N. P. Armitage, E. J. Mele, and A. Vishwanath, Weyl and Dirac semimetals in three-dimensional solids, Rev. Mod. Phys. **90**, 015001 (2018).

[8] B. Q. Lv, T. Qian, and H. Ding, Experimental perspective on three-dimensional topological semimetals, Rev. Mod. Phys. **93**, 025002 (2021).

[9] D. Hsieh, D. Qian, L. Wray, Y. Xia, Y. S. Hor, R. J. Cava, and M. Z. Hasan, A topological Dirac insulator in a quantum spin Hall phase, Nature (London) **452**, 970 (2008).

[10] S. Xu, Y. Xia, L. A. Wray, S. Jia, F. Meier, J. H. Dil, J. Osterwalder, B. Slomski, A. Bansil, H. Lin, R. J. Cava, and M. Z. Hasan, Topological phase transition and texture inversion in a tunable topological insulator, Science **332**, 560 (2011).

[11] X. Xi, C. Ma, Z. Liu, Z. Chen, W. Ku, H. Berger, C. Martin, D. B. Tanner, and G. L. Carr, Signatures of a pressure-induced topological quantum phase transition in BiTeI, Phys. Rev. Lett. **111**, 155701 (2013).

[12] A. Bera, K. Pal, D. V. S. Muthu, S. Sen, P. Guptasarma, U. V. Waghmare, and A. K. Sood, Sharp Raman anomalies and broken adiabaticity at a pressure induced transition from band to topological insulator in Sb_2Se_3, Phys. Rev. Lett. **110**, 107401 (2013).

[13] Y. Liu, Y. Y. Li, S. Rajput, D. Gilks, L. Lari, P. L. Galindo, V. K. Weinert, M. Lazarov, and V. K. Li, Tuning Dirac states by strain in the topological insulator Bi_2Se_3, Nat. Phys. **10**, 294 (2014).

[14] S. Liu, Y. Kim, L. Z. Tan, and A. M. Rappe, Strain-induced ferroelectric topological insulator, Nano Lett. **16**, 1663 (2016).

[15] X. Lin and J. Ni, Topological phase transition due to strain-controlled evolution of the inverted bands in $1T'$-MX_2, Phys. Rev. B **95**, 245436 (2017).

[16] M. Kim, C. H. Kim, H. Kim, and J. Ihm, Topological quantum phase transitions driven by external electric fields in Sb_2Te_3 thin films, Proc. Natl. Acad. Sci. USA **109**, 671 (2012).

[17] T. Zhang, J. Ha, N. Levy, Y. Kuk, and J. Stroscio, Electric-field tuning of the surface band structure of topological insulator Sb_2Te_3 thin films, Phys. Rev. Lett. **111**, 056803 (2013).

[18] X. Lin and J. Ni, Switch effect of the nonquantized intrinsic spin Hall conductivity in monolayered monoclinic transition metal dichalcogenides, J. Phys.: Condens. Matter **29**, 295302 (2017).

[19] I. Garate, Phonon-induced topological transitions and crossovers in Dirac materials, Phys. Rev. Lett. **110**, 046402 (2013).

[20] K. Saha and I. Garate, Phonon-induced topological insulation, Phys. Rev. B **89**, 205103 (2014).

[21] B. Monserrat and D. Vanderbilt, Temperature effects in the band structure of topological insulators, Phys. Rev. Lett. **117**, 226801 (2016).

[22] G. Antonius and S. G. Louie, Temperature-induced topological phase transitions: Promoted versus suppressed nontrivial topology, Phys. Rev. Lett. **117**, 246401 (2016).

[23] B. Monserrat and A. Narayan, Unraveling the topology of $ZrTe_5$ by changing temperature, Phys. Rev. Res. **1**, 033181 (2019).

[24] B. Peng, I. Bravić, J. L. MacManus-Driscoll, and B. Monserrat, Topological semimetallic phase in PbO_2 promoted by temperature, Phys. Rev. B **100**, 161101(R) (2019).

[25] V. Brousseau-Couture, G. Antonius, and M. Côté, Temperature dependence of the topological phase transition of BiTeI from first principles, Phys. Rev. Res. **2**, 023185 (2020).

[26] J. D. Querales-Flores, P. Aguado-Puente, Đorđe Dangić, J. Cao, P. Chudzinski, T. N. Todorov, M. Grüning, S. Fahy, and I. Savić, Towards temperature-induced topological phase transition in SnTe: A first-principles study, Phys. Rev. B **101**, 235206 (2020).

[27] S. Chen, P. T. Salzbrenner, and B. Monserrat, Nonuniform grids for Brillouin zone integration and interpolation, Phys. Rev. B **106**, 155102 (2022).

[28] A. Marrazzo, Thermal robustness of the quantum spin Hall phase in monolayer WTe_2, Phys. Rev. Mater. **7**, L021201 (2023).

[29] S. Wiedmann, A. Jost, C. Thienel, C. Brüne, P. Leubner, H. Buhmann, L. W. Molenkamp, J. C. Maan, and U. Zeitler, Temperature-driven transition from a semiconductor to a topological insulator, Phys. Rev. B **91**, 205311 (2015).

[30] B. M. Wojek, M. H. Berntsen, V. Jonsson, A. Szczerbakow, P. Dziawa, B. J. Kowalski, T. Story, and O. Tjernberg, Direct observation and temperature control of the surface Dirac gap in a topological crystalline insulator, Nat. Commun. **6**, 8463 (2015).

[31] S. Thirupathaiah, R. Jha, B. Pal, J. S. Matias, P. K. Das, I. Vobornik, R. A. Ribeiro, and D. D. Sarma, Temperature-independent band structure of WTe$_2$ as observed from angle-resolved photoemission spectroscopy, Phys. Rev. B **96**, 165149 (2017).

[32] A. N. Berger, E. Andrade, A. Kerelsky, D. Edelberg, J. Li, Z. Wang, L. Zhang, J. Kim, N. Zaki, J. Avila, C. Chen, M. C. Asensio, S.-W. Cheong, B. A. Bernevig, and A. N. Pasupathy, Temperature-driven topological transition in 1T′-MoTe$_2$, npj Quantum Mater. **3**, 2 (2018).

[33] Y. J. Chen, L. X. Xu, J. H. Li, Y. W. Li, H. Y. Wang, C. F. Zhang, H. Li, Y. Wu, A. J. Liang, C. Chen, S. W. Jung, C. Cacho, Y. H. Mao, S. Liu, M. X. Wang, Y. F. Guo, Y. Xu, Z. K. Liu, L. X. Yang, and Y. L. Chen, Topological electronic structure and its temperature evolution in antiferromagnetic topological insulator MnBi$_2$Te$_4$, Phys. Rev. X **9**, 041040 (2019).

[34] S. Regmi, M. M. Hosen, B. Ghosh, B. Singh, G. Dhakal, C. Sims, B. Wang, F. Kabir, K. Dimitri, Y. Liu, A. Agarwal, H. Lin, D. Kaczorowski, A. Bansil, and M. Neupane, Temperature-dependent electronic structure in a higher-order topological insulator candidate EuIn$_2$As$_2$, Phys. Rev. B **102**, 165153 (2020).

[35] D. A. Estyunin, I. I. Klimovskikh, A. M. Shikin, E. F. Schwier, M. M. Otrokov, A. Kimura, S. Kumar, S. O. Filnov, Z. S. Aliev, M. B. Babanly, and E. V. Chulkov, Signatures of temperature driven antiferromagnetic transition in the electronic structure of topological insulator MnBi$_2$Te$_4$, APL Mater. **8**, 021105 (2020).

[36] Y. Jiang, T. Zhao, L. Zhang, Q. Chen, H. Zhou, M. Ozerov, D. Smirnov, and Z. Jiang, Revealing temperature evolution of the Dirac band in ZrTe$_5$ via magnetoinfrared spectroscopy, Phys. Rev. B **108**, L041202 (2023).

[37] I. Mohelsky, J. Wyzula, B. A. Piot, G. D. Gu, Q. Li, A. Akrap, and M. Orlita, Temperature dependence of the energy band gap in ZrTe$_5$: Implications for the topological phase, Phys. Rev. B **107**, L041202 (2023).

[38] X. Qian, J. Liu, L. Fu, and J. Li, Quantum spin Hall effect in two-dimensional transition metal dichalcogenides, Science **346**, 1344 (2014).

[39] S. Tang, C. Zhang, D. Wong, Z. Pedramrazi, H.-Z. Tsai, C. Jia, B. Moritz, M. Claassen, H. Ryu, S. Kahn, J. Jiang, H. Yan, M. Hashimoto, D. Lu, R. G. Moore, C.-C. Hwang, C. Hwang, Z. Hussain, Y. Chen, M. M. Ugeda, Z. Liu, X. Xie, T. P. Devereaux, M. F. Crommie, S.-K. Mo, and Z.-X. Shen, Quantum spin Hall state in monolayer 1T′-WTe$_2$, Nat. Phys. **13**, 683 (2017).

[40] S. Murakami, S. Iso, Y. Avishai, M. Onoda, and N. Nagaosa, Tuning phase transition between quantum spin Hall and ordinary insulating phases, Phys. Rev. B **76**, 205304 (2007).

[41] P. B. Allen and V. Heine, Theory of the temperature dependence of electronic band structures, J. Phys. C: Solid State Phys. **9**, 2305 (1976).

[42] P. B. Allen and M. Cardona, Theory of the temperature dependence of the direct gap of germanium, Phys. Rev. B **23**, 1495 (1981).

[43] P. B. Allen and M. Cardona, Temperature dependence of the direct gap of Si and Ge, Phys. Rev. B **27**, 4760 (1983).

[44] S. Poncé, G. Antonius, Y. Gillet, P. Boulanger, J. Laflamme Janssen, A. Marini, M. Côté, and X. Gonze, Temperature dependence of electronic eigenenergies in the adiabatic harmonic approximation, Phys. Rev. B **90**, 214304 (2014).

[45] B. Monserrat, Electron-phonon coupling from finite differences, J. Phys.: Condens. Matter **30**, 083001 (2018).

[46] F. Giustino, Electron-phonon interactions from first principles, Rev. Mod. Phys. **89**, 015003 (2017).

[47] H. Fröhlich, H. Pelzer, and S. Zienau, XX. properties of slow electrons in polar materials, Philos. Mag. **41**, 221 (1950).

[48] H. Fröhlich, Electrons in lattice fields, Adv. Phys. **3**, 325 (1954).

[49] C. Verdi and F. Giustino, Fröhlich electron-phonon vertex from first principles, Phys. Rev. Lett. **115**, 176401 (2015).

[50] J. P. Nery and P. B. Allen, Influence of Fröhlich polaron coupling on renormalized electron bands in polar semiconductors: Results for zinc-blende GaN, Phys. Rev. B **94**, 115135 (2016).

[51] W. H. Sio and F. Giustino, Unified *ab initio* description of Fröhlich electron-phonon interactions in two-dimensional and three-dimensional materials, Phys. Rev. B **105**, 115414 (2022).

[52] W. H. Sio and F. Giustino, Polarons in two-dimensional atomic crystals, Nat. Phys. **19**, 629 (2023).

[53] J. H. Lloyd-Williams and B. Monserrat, Lattice dynamics and electron-phonon coupling calculations using nondiagonal supercells, Phys. Rev. B **92**, 184301 (2015).

[54] G. Leibfried and W. Ludwig, Theory of anharmonic effects in crystals, Solid State Phys. **12**, 275 (1961).

[55] A. Singh, S. N. Shirodkar, and U. V. Waghmare, 1H and 1T polymorphs, structural transitions and anomalous properties of (Mo,W)(S,Se)$_2$ monolayers: First-principles analysis, 2D Mater. **2**, 035013 (2015).

[56] S. S. Chou, N. Sai, P. Lu, E. N. Coker, S. Liu, K. Artyushkova, T. S. Luk, B. Kaehr, and C. J. Brinker, Understanding catalysis in a multiphasic two-dimensional transition metal dichalcogenide, Nat. Commun. **6**, 8311 (2015).

[57] P. Hohenberg and W. Kohn, Inhomogeneous electron gas, Phys. Rev. **136**, B864 (1964).

[58] W. Kohn and L. J. Sham, Self-consistent equations including exchange and correlation effects, Phys. Rev. **140**, A1133 (1965).

[59] G. Kresse and J. Furthmüller, Efficiency of ab-initio total energy calculations for metals and semiconductors using a plane-wave basis set, Comput. Mater. Sci. **6**, 15 (1996).

[60] P. E. Blöchl, Projector augmented-wave method, Phys. Rev. B **50**, 17953 (1994).

[61] G. Kresse and D. Joubert, From ultrasoft pseudopotentials to the projector augmented-wave method, Phys. Rev. B **59**, 1758 (1999).

[62] J. P. Perdew, K. Burke, and M. Ernzerhof, Generalized gradient approximation made simple, Phys. Rev. Lett. **77**, 3865 (1996).

[63] A. V. Krukau, O. A. Vydrov, A. F. Izmaylov, and G. E. Scuseria, Influence of the exchange screening parameter on the perfor-

mance of screened hybrid functionals, J. Chem. Phys. **125**, 224106 (2006).

[64] D. D. Koelling and B. N. Harmon, A technique for relativistic spin-polarised calculations, J. Phys. C: Solid State Phys. **10**, 3107 (1977).

[65] M. M. Ugeda, A. Pulkin, S. Tang, H. Ryu, Q. Wu, Y. Zhang, D. Wong, Z. Pedramrazi, A. Martín-Recio, Y. Chen, F. Wang, Z.-X. Shen, S.-K. Mo, O. V. Yazyev, and M. F. Crommie, Observation of topologically protected states at crystalline phase boundaries in single-layer WSe$_2$, Nat. Commun. **9**, 3401 (2018).

[66] H. Xu, D. Han, Y. Bao, F. Cheng, Z. Ding, S. J. R. Tan, and K. P. Loh, Observation of gap opening in 1T′ phase MoS$_2$ nanocrystals, Nano Lett. **18**, 5085 (2018).

[67] P. Chen, W. W. Pai, Y.-H. Chan, W.-L. Sun, C.-Z. Xu, D.-S. Lin, M. Y. Chou, A.-V. Fedorov, and T.-C. Chiang, Large quantum-spin-Hall gap in single-layer 1T′ WSe$_2$, Nat. Commun. **9**, 2003 (2018).

[68] L. Jelver, D. Stradi, K. Stokbro, T. Olsen, and K. W. Jacobsen, Spontaneous breaking of time-reversal symmetry at the edges of 1T′ monolayer transition metal dichalcogenides, Phys. Rev. B **99**, 155420 (2019).

[69] J. Cayssol and J. N. Fuchs, Topological and geometrical aspects of band theory, J. Phys. Mater. **4**, 034007 (2021).

[70] L. Xu, Y. Li, Y. Fang, H. Zheng, W. Shi, C. Chen, D. Pei, D. Lu, M. Hashimoto, M. Wang, L. Yang, X. Feng, H. Zhang, F. Huang, Q. Xue, K. He, Z. Liu, and Y. Chen, Topology hierarchy of transition metal dichalcogenides built from quantum spin Hall layers, Adv. Mater. **35**, 2300227 (2023).

[71] B. Das, D. Sen, and S. Mahapatra, Tuneable quantum spin Hall states in confined 1T′ transition metal dichalcogenides, Sci. Rep. **10**, 6670 (2020).

[72] See Supplemental Material at http://link.aps.org/supplemental/10.1103/PhysRevB.109.155125 for Fig. S1 for the phonon dispersions. The figure also visualizes the acoustic flexural (an important feature of 2D materials, see also Ref. [90] therein) and longitudinal optical modes near the Γ point.

[73] J. P. Perdew, W. Yang, K. Burke, Z. Yang, E. K. U. Gross, M. Scheffler, G. E. Scuseria, T. M. Henderson, I. Y. Zhang, A. Ruzsinszky, H. Peng, J. Sun, E. Trushin, and A. Görling, Understanding band gaps of solids in generalized Kohn-Sham theory, Proc. Natl. Acad. Sci. USA **114**, 2801 (2017).

[74] See Supplemental Material at http://link.aps.org/supplemental/10.1103/PhysRevB.109.155125 for Fig. S2 for the quantitative comparison of the electron-phonon coupling strength associated with Γ and X phonons at the PBE and HSE levels.

[75] G. Antonius, S. Poncé, P. Boulanger, M. Côté, and X. Gonze, Many-body effects on the zero-point renormalization of the band structure, Phys. Rev. Lett. **112**, 215501 (2014).

[76] B. Monserrat, Correlation effects on electron-phonon coupling in semiconductors: Many-body theory along thermal lines, Phys. Rev. B **93**, 100301(R) (2016).

[77] See Supplemental Material at http://link.aps.org/supplemental/10.1103/PhysRevB.109.155125 for Fig. S3 for the detailed convergence tests of band gap renormalization.

[78] W. R. L. Lambrecht, C. Bhandari, and M. van Schilfgaarde, Lattice polarization effects on the screened Coulomb interaction W of the GW approximation, Phys. Rev. Mater. **1**, 043802 (2017).

[79] See Supplemental Material at http://link.aps.org/supplemental/10.1103/PhysRevB.109.155125 for Fig. S4 for the thermal expansion of WS$_2$, WSe$_2$, MoS$_2$, and MoSe$_2$ as a function of temperature.

[80] Y. P. Varshni, Temperature dependence of the energy gap in semiconductors, Physica **34**, 149 (1967).

[81] See Supplemental Material at http://link.aps.org/supplemental/10.1103/PhysRevB.109.155125 for Fig. S5 and Table S1 for the fitted models and the values of corresponding fitted parameters.

[82] M. Born, K. Huang, and M. Lax, *Dynamical Theory of Crystal Lattices* (Oxford University Press, Oxford, England, UK, 1955).

[83] M. T. Dove, *Introduction to Lattice Dynamics* (Cambridge University Press, Cambridge, England, UK, 1993).

[84] F. Giustino, S. G. Louie, and M. L. Cohen, Electron-phonon renormalization of the direct band gap of diamond, Phys. Rev. Lett. **105**, 265501 (2010).

[85] F. Giustino, M. L. Cohen, and S. G. Louie, Electron-phonon interaction using Wannier functions, Phys. Rev. B **76**, 165108 (2007).

[86] B. M. Deb, Note on an upper bound property of second derivatives of the energy, Chem. Phys. Lett. **17**, 78 (1972).

[87] S. Baroni, S. de Gironcoli, A. Dal Corso, and P. Giannozzi, Phonons and related crystal properties from density-functional perturbation theory, Rev. Mod. Phys. **73**, 515 (2001).

[88] S. Poncé, Y. Gillet, J. Laflamme Janssen, A. Marini, M. Verstraete, and X. Gonze, Temperature dependence of the electronic structure of semiconductors and insulators, J. Chem. Phys. **143**, 102813 (2015).

[89] J. Callaway, *Quantum Theory of the Solid State* (Academic Press, Cambridge, MA, 1976).

[90] J.-W. Jiang, B.-S. Wang, J.-S. Wang, and H. S. Park, A review on the flexural mode of graphene: Lattice dynamics, thermal conduction, thermal expansion, elasticity and nanomechanical resonance, J. Phys.: Condens. Matter **27**, 083001 (2015).